Development of a high-alloyed duplex stainless steel with enhanced mechanical property and corrosion resistance

Citation for the original published paper (version of record):
Ma, D., Yao, X., Zhang, H. et al (2026). Development of a high-alloyed duplex stainless steel with enhanced mechanical property and
corrosion resistance. Journal of Materials Research and Technology, 42: 10079-10088.
http://dx.doi.org/10.1016/j.jmrt.2026.05.267

Journal of Materials Research and Technology 42 (2026) 10079–10088

Contents lists available at ScienceDirect

Journal of Materials Research and Technology

journal homepage: www.elsevier.com/locate/jmrt

Development of a high-alloyed duplex stainless steel with enhanced mechanical property and corrosion resistance

Dong Ma [a,c,1], Xunjie Yao [a,1], Hui Zhang [a,*], Hu Lei [a], Jicheng Ding [a], Sheng Guo [b]

[a] School of Materials Science and Engineering, Anhui University of Technology, Ma'anshan, 243002, Anhui, China
[b] Department of Industrial and Materials Science, Chalmers University of Technology, SE-41296, Gothenburg, Sweden
[c] School of Materials Science and Engineering, Zhejiang University, Hangzhou, 310027, China

ARTICLE INFO

Keywords:
Duplex stainless steel
High alloying effect
Tensile property
Corrosion resistance
Nano-precipitates

ABSTRACT

Duplex stainless steels (DSSs) are attractive structural materials because of their excellent corrosion resistance and favorable strength–ductility balance. In this study, a novel high-alloyed duplex stainless steel (HA-DSS) with a nominal composition of $Fe_{60}Cr_{18}Co_6Ni_6Mo_6Cu_4$ was developed. After solution treatment at 1180 °C, the alloy exhibited a balanced duplex microstructure with BCC and FCC phase fractions of approximately 54% and 46%, respectively. Under this condition, the alloy achieved a tensile strength of 763 MPa and an elongation of 24%. Compared with commercial 2205-DSS, the optimized HA-DSS showed significantly improved corrosion resistance. In 3.5 wt% NaCl solution, the HA-DSS exhibited a higher corrosion potential (−0.250 V vs. −0.354 V), a lower corrosion current density (0.299 μA cm^{-2} vs. 0.909 μA cm^{-2}), and a higher pitting potential (1.09 V vs. 1.01 V). In 10 wt% H_2SO_4 solution, it also showed a higher corrosion potential (−0.230 V vs. −0.269 V) and a markedly lower corrosion current density (15.33 μA cm^{-2} vs. 69.99 μA cm^{-2}). X-ray photoelectron spectroscopy revealed that Co, Mo, and Cu contributed synergistically to the improved passive-film characteristics. Transmission electron microscopy further showed abundant dislocations in the FCC phase and nanoscale Cu-rich precipitates in the BCC phase, which contributed to the enhanced mechanical performance. These results demonstrate that the proposed HA-DSS provides an effective strategy for simultaneously improving duplex phase stability, mechanical properties, and corrosion resistance.

1. Introduction

Duplex stainless steels (DSS), characterized by an approximately equal proportion of face-centered cubic (FCC) and body-centered cubic (BCC) phases, showcase excellent corrosion resistance and a decent balance of strength and plasticity, positioning themselves as a viable alternative to traditional high-performance austenitic or ferritic stainless steels [1–4].

DSS is a type of heavily alloyed steels engineered to finely balance the proportion of their two phases, typically aiming for an approximately equal ratio to optimize the overall performance, i.e., corrosion resistance and mechanical properties. Over the years, different alloying strategies have been explored to improve the overall performance of DSS. For example, Pan et al. found that adding 0.5% Cu increased the solid solubility of Cr in the Fe–Cr–Mn–Al DSS, hence improving its pitting resistance [5]; Yoon et al. noticed that adding Mo with the large atomic radius to the DSS enhanced solid solution strengthening, suppressed the Cr_2N precipitation, enhanced the FCC phase stability, improved the passivation ability, and also significantly reduced the elongation reduction after aging [6]; furthermore, adding Co was considered a viable strategy to substitute Ni, which not only enhanced the corrosion resistance but also impeded the formation of grain boundary precipitates [7]. Nevertheless, there has been a long-standing concern that the addition of excessive alloying elements would promote the formation of intermetallic phases (e.g., δ, χ, σ, R, and π phases), which can severely degrade both toughness and corrosion resistance of heavily alloyed steels [8]. This challenge is also faced by highly alloyed DSS in their pursuit of enhanced performance [8,9].

In recent years, there has been strong research interest in high-entropy alloys (HEAs) or medium-entropy alloys (MEAs). Notably, dual-phase HEAs/MEAs containing both FCC and BCC phases present an appealing combination of exceptional corrosion resistance and superior

* Corresponding author.
E-mail address: huizhang@ahut.edu.cn (H. Zhang).
[1] The two authors contributed equally to this work.

https://doi.org/10.1016/j.jmrt.2026.05.267
Received 30 March 2025; Received in revised form 20 March 2026; Accepted 25 May 2026
Available online 25 May 2026

mechanical properties. For example, Wang et al. developed a series of duplex Co-rich HEAs (FCC + HCP) that effectively overcome the strength-ductility trade-off through the thermally induced HCP phase, exhibiting superior corrosion resistance and strong passivation ability [10]; Lim et al. proposed an ultra-high-strength duplex Al–Co–Cr–Fe–Ni HEA with an impressive tensile strength of 1031 MPa and reasonable tensile ductility after aging, due to B2 particles reinforcing the hierarchical α (BCC)-matrix [11]. Numerous studies have underscored the effectiveness of duplex structures in achieving optimal performance [12–14]. More recently, the efficacy of the medium-entropy effect in maintaining a simple solid solution phase over intermetallic compounds has been revealed in a series of high-alloyed stainless steels (HASS) [15–17], where the alloying strategy of HEAs/MEAs is adopted. Typically, FCC-structured HASS demonstrate lower hardness than BCC-structured HASS, with or without precipitation hardening [15], while BCC-structured HASS with a high hardness normally fail to achieve the necessary levels of plasticity and toughness required for industrial applications [16,17]. How to achieve balanced mechanical properties in HASS remains to be a challenge. In addition, a challenge for the industrial application of duplex HASS lies in their high material costs. In this study, we developed a novel high-alloyed duplex stainless steel (HA-DSS) with a nominal composition of $Fe_{60}Cr_{18}Co_6Ni_6Mo_6Cu_4$. The alloy design was inspired by both the advancements in HEAs/MEAs and the known characteristics of conventional high-alloyed, ultra-low carbon DSS. Based on an Fe–Cr matrix, near-equiatomic proportions of Co, Ni, Mo, and Cu were added, leveraging the sluggish diffusion effect of entropy-stabilized systems to suppress the formation of intermetallic phases. This allows better control of the austenite/ferrite ratio and enhances corrosion resistance, particularly in chloridic and acidic environments. Compared with 2205-DSS, our designed HA-DSS exhibited improved mechanical properties and corrosion resistance both in NaCl and H_2SO_4 solutions, making it a promising candidate in such corrosive environments. Moreover, since the HA-DSS contains copper, which is known to exhibit excellent antibacterial properties in steels, the alloy also holds potential for bio-corrosion resistance in marine environments or even antibacterial function in biomedical applications.

2. Materials and methods

2.1. Materials design

The design of HA-DSS composition was guided by several key considerations. Firstly, the composition was designed based on a combination of stainless steel design principle and the medium-entropy alloy (MEA) concept. When the Cr content exceeds 12 wt%, a stable passive film forms on the steel surface. Increasing Cr content improves the passive film's performance; conventional austenitic stainless steels typically contain ~18 wt% Cr, while duplex stainless steels (DSSs) often contain ~21 wt% Cr. In our design, the Cr content is set as 18 wt%. Secondly, near-equiatomic additions of Co, Ni, Mo, and Cu were added to explore entropic effects hoping to suppress the intermetallic phase formation, and to enhance corrosion and mechanical performance. Co contributes to significant lattice distortion, enhancing solid solution strengthening and corrosion resistance [7]; Ni is a strong austenite stabilizer; Mo favors ferrite formation and improves pitting resistance by enhancing the passive film stability, particularly under chloridic environments; Cu, although not traditionally used in stainless steels, has recently widely been recognized for its role in enhancing antibacterial corrosion resistance. It can also increase Cr solubility in austenite and improve pitting resistance. However, excess Cu may cause embrittlement, so its content was limited to 4 at.%.

Thirdly, a set of empirical parameters was employed to achieve the dual-phase structure of the HA-DSS, which were typically used in the design of HEAs/MEAs and traditional stainless steels. One critical parameter was the valence electron concentration (VEC). When the VEC value falls within the range of 6.87 to 8, it suggests the potential to form a combination of FCC and BCC phases in HEAs/MEAs [18]. In our target HA-DSS composition, the calculated VEC is 7.82, which indicates that the formation of a duplex structure is favorable. Fourthly, the calculated Cr_{eq}/Ni_{eq} ratio is 2.3, derived using the following empirical equations [19]:

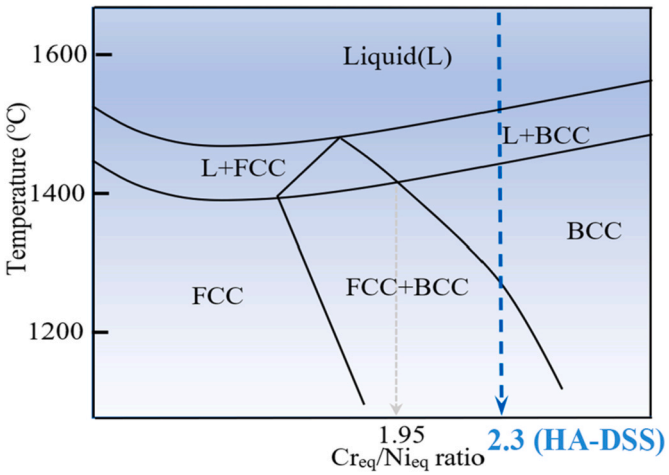

Fig. 1. The Schaeffler phase diagram of steels based on the Cr_{eq}/Ni_{eq} ratio [19].

$$Cr_{eq} = \omega(Cr) + 1.5\omega(Mo) + 1.5\omega(Si) + 0.5\omega(Nb) \quad (1)$$

$$Ni_{eq} = \omega(Ni) + \omega(Co) + 0.5\omega(Mn) + 0.3\omega(Cu) \quad (2)$$

where the concentrations of the respective elements given in parentheses are in weight percentage. Here, Cr_{eq} represents the ferrite (BCC) stabilizing chromium equivalent, and Ni_{eq} represents the austenite (FCC) stabilizing nickel equivalent. The calculated values of chromium and nickel equivalents for the target HA-DSS are 30.91 wt % and 13.43 wt%, respectively. As shown in the Schaeffler phase diagram for Cr/Ni equivalent in Fig. 1, the designed HA-DSS would be a dual-phase structure containing both FCC and BCC phases.

2.2. Experiment methods

The HA-DSS ingots with a nominal composition of $Fe_{60}Cr_{18}Co_6Ni_6Mo_6Cu_4$ (at.%) were prepared by arc melting high-purity raw elements (purity >99.9 wt%) in an argon atmosphere using a WK-II type electric arc melting furnace (Beijing Wuke Optoelectronic Technology Co., Ltd., China). All ingots were remelted at least five times to ensure chemical homogeneity and then drop-cast into a water-cooled copper mold with a diameter of 50 mm. The resulting cast ingots had a diameter of approximately 23 mm and a mass of ~20 g per sample. For comparison, a widely used commercial SAF 2205 duplex stainless steel (2205-DSS) was purchased and remelted following the same arc-melting procedure. The composition of the 2205-DSS, determined by spectroscopic analysis, was Cr: 21.83%, Ni: 5.45%, Mo: 3.09%, Mn: 1.13%, C: 0.03%, Si: 0.58%, N: 0.17%, and Fe: balance (wt.%).

Solution treatment is a common and essential process for stainless steels, especially duplex stainless steels (DSSs), where it plays a critical role in achieving a balanced dual-phase microstructure. The optimal combination of corrosion resistance and mechanical properties is generally obtained when the volume fractions of ferrite and austenite are close to 1:1. Therefore, in this study, solution treatments were carried out at four temperatures (1030 °C, 1080 °C, 1130 °C, and 1180 °C), selected within the typical solution-treatment temperature range of 2205 DSS (typically 1020–1200 °C, as reported in the literature [20–22]). These temperatures were chosen at 50 °C intervals to systematically investigate the evolution of phase balance and to identify the optimal temperature for obtaining the desired duplex structure.

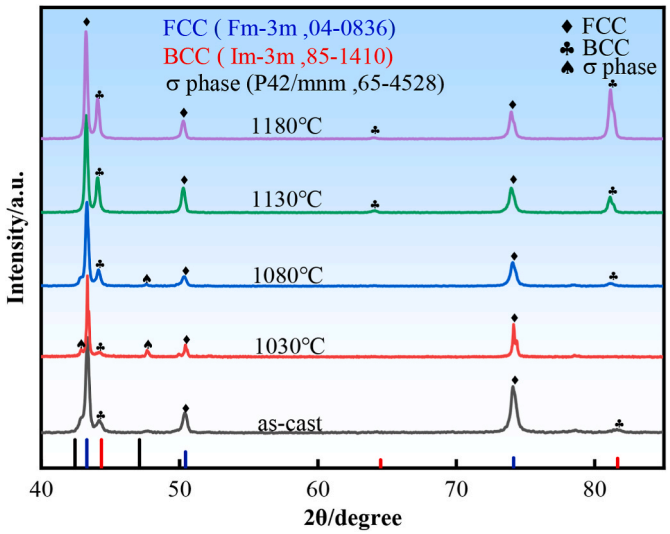

Fig. 2. The XRD patterns of the HA-DSS at the as-cast state and after solution treatment at different temperatures.

Multiscale characterization techniques were employed to investigate the microstructural evolution and elemental distribution of the HA-DSS after different heat treatments, including X-ray diffraction (XRD, D8 Advance, Bruker, Germany) with Cu Kα radiation, field-emission scanning electron microscopy (FE-SEM, Quanta 450, FEI, USA) equipped with electron backscatter diffraction (EBSD, Oxford Instruments, UK) and energy-dispersive spectroscopy (EDS, Oxford Instruments, UK), and transmission electron microscopy (TEM, Tecnai G2 F20 STWIN, FEI, The Netherlands). The volume fractions of the BCC and FCC phases were determined from SEM micrographs by quantitative image analysis. A mixed acid etchant (30 mL HCl + 10 mL H_2SO_4) was used to reveal the duplex-phase boundaries.

To ensure comparable elongation data according to proportional specimen standards (ISO 6892-1), sub-sized flat tensile specimens with a gauge length of 8 mm and a cross-section of 1 mm × 2 mm were machined. The tests were conducted using a universal testing machine (Instron 5565, Instron, USA) at an initial strain rate of 5×10^{-4} s^{-1} at room temperature. To ensure reproducibility, two tensile specimens of identical dimensions were prepared and tested for each condition. The corrosion properties were quantitatively evaluated by potentiodynamic polarization using an electrochemical workstation (CHI604D, Shanghai Chenhua Instrument Co., Ltd., China). The test alloys served as the working electrode with an exposed surface area of 10 mm × 10 mm, while a platinum plate and a saturated calomel electrode (SCE) were used as the counter electrode and reference electrode, respectively. Immersion corrosion tests were also conducted in 45 wt% H_2SO_4 solution at 60 °C for 9 h. The corrosion behavior after immersion was qualitatively evaluated by comparing the changes in specimen surface condition, specimen size, and solution appearance. X-ray photoelectron spectroscopy (XPS, K-Alpha, Thermo Fisher Scientific, USA) with a monochromatic Al Kα source was used to analyze the elemental composition of the surface passive film.

3. Results and discussion

3.1. Phases and microstructure evolution after solution treatment

The XRD patterns shown in Fig. 2 indicate that the HA-DSS exhibits a dual-phase microstructure composed of FCC and BCC phases. With an increase in the solution treatment temperature, there is an obvious enhancement in the peak intensity of the BCC phase, which confirms the transition from the FCC phase to the BCC phase. Furthermore, it should be noted that the σ phase precipitates after solution treatment at 1030 °C, but its precipitation can be avoided with higher temperature solution treatment at 1130 °C and 1180 °C. The σ phase is commonly found in traditional DSS and is believed to harm corrosion resistance and ductility [23,24].

Fig. 3 shows the microstructure of the HA-DSS in the as-cast state. The solidification sequence seems to follow L→L + BCC→BCC→BCC + FCC, which aligns with the typical solidification behavior of conventional DSS as indicated in the Schaeffler phase diagram shown in Fig. 1. The BCC phase is the primary phase that forms directly from the liquid [19]. Below the BCC phase solvus line, a transformation from the BCC phase to the FCC phase occurs in the solid state. The FCC phase starts to nucleate at the BCC grain boundaries (GB) with higher Gibbs free energy, referred to as GB-FCC as marked by blue dotted lines in Fig. 3(a–b). Subsequently, more intragranular FCC phases nucleate within the BCC

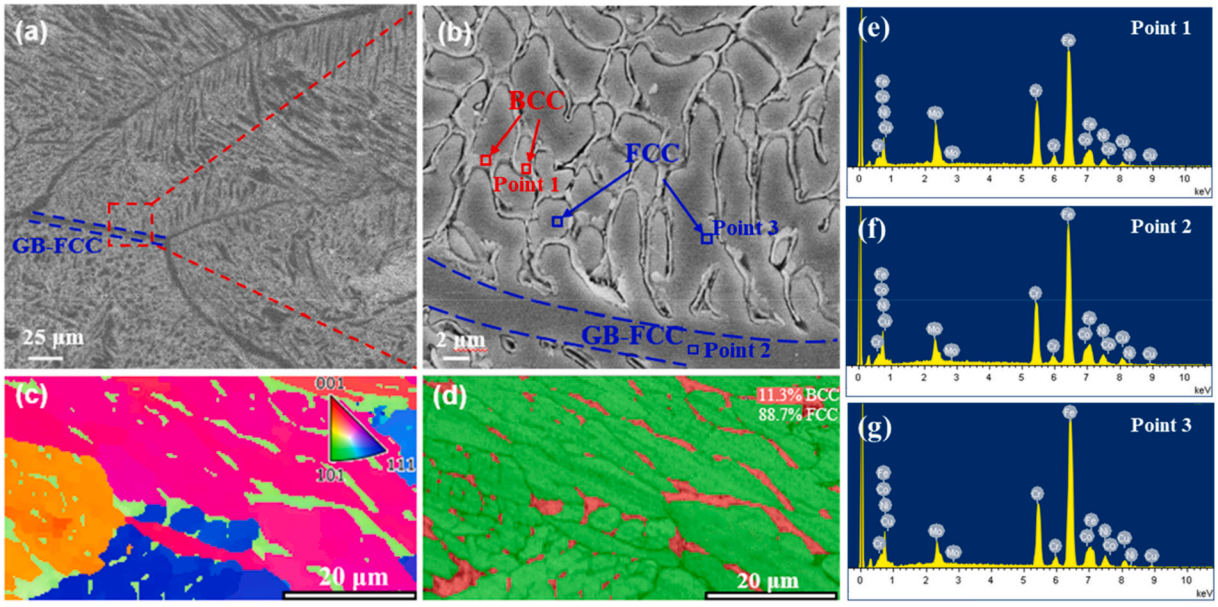

Fig. 3. The microstructure of the HA-DSS in the as-cast state: (a-b) SEM microstructure; (c-d) IPF and phase map by EBSD; (e-g) EDS spectra of the three points marked in (b).

Table 1
EDS analysis for the HA-DSS at the as-cast state and after solution treatment at 1180 °C, all in at.%.

State	Phases	Fe	Cr	Co	Ni	Mo	Cu
As-cast	BCC	55.17	21.56	5.08	4.66	10.89	2.64
	FCC	59.74	17.85	6.56	6.31	5.34	4.20
	GB-FCC	59.38	18.43	5.84	6.18	6.00	4.17
1180 °C	BCC	51.82	20.83	5.3	4.8	14.62	2.63
	FCC	59.15	18.17	6.36	6.74	5.53	4.05

matrix, while the remaining untransformed BCC phases create a network. The inverse pole figure (IPF) and phase map obtained from the EBSD observation in Fig. 3(c–d) prove that the FCC phases formed within each original BCC grain exhibit nearly identical orientation. In contrast, the orientations of the FCC phases nucleated within different original BCC grains are distinctly different. After solidification, the remaining BCC phases account for about 11.3 % of the total content. The corresponding EDS analysis in Table 1 reveals that the corrosion-resistant elements like Co, Ni, and Cr are almost equally distributed in the two phases. In contrast, Mo is more concentrated in the BCC phase, while the contents of Cu and Fe are slightly higher in the FCC phase. The corresponding EDS spectra are presented in Fig. 3(e–g).

Fig. 4 presents the microstructure evolution after solution treatment. Fig. 4(a) presents that while the GB-FCC is still visible, the network-shaped BCC phase begins to break apart, forming long or short rods after solution treatment at 1030 °C. In Fig. 4(b–d) with increasing the solution treatment temperature, the volume fraction of the BCC phase gradually increases and reaches about 46% at 1180 °C, as determined from image analysis, approaching an approximately equal proportion of both phases. Table 1 compares the EDS data and indicates a more uniform elemental distribution after solution treatment at 1180 °C. The corresponding EDS spectra are presented in Fig. 4(e and f).

3.2. *Tensile property and strengthening mechanism of the HA-DSS*

Fig. 5 (a) shows the engineering tensile stress-strain curves of the HA-DSS. The as-cast HA-DSS exhibits a higher tensile elongation of 38%. As the solution treatment temperature rises, the strength increases

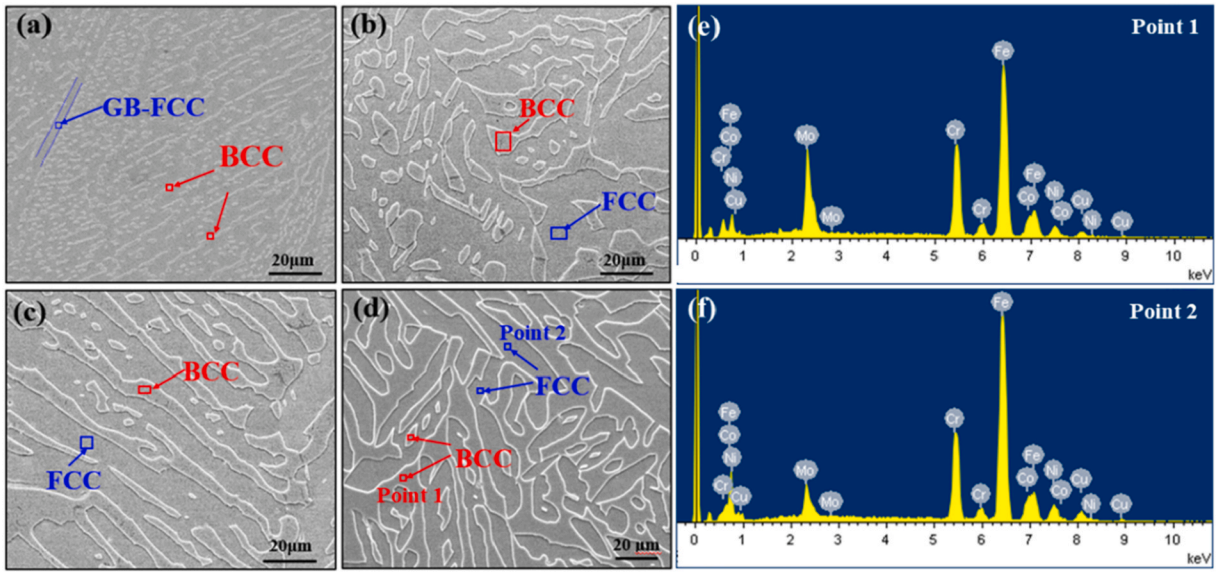

Fig. 4. The microstructure of the HA-DSS after solution treatment: (a) 1030 °C; (b) 1080 °C; (c) 1130 °C; (d) 1180 °C. (e-f) EDS spectra of the three points marked in (b).

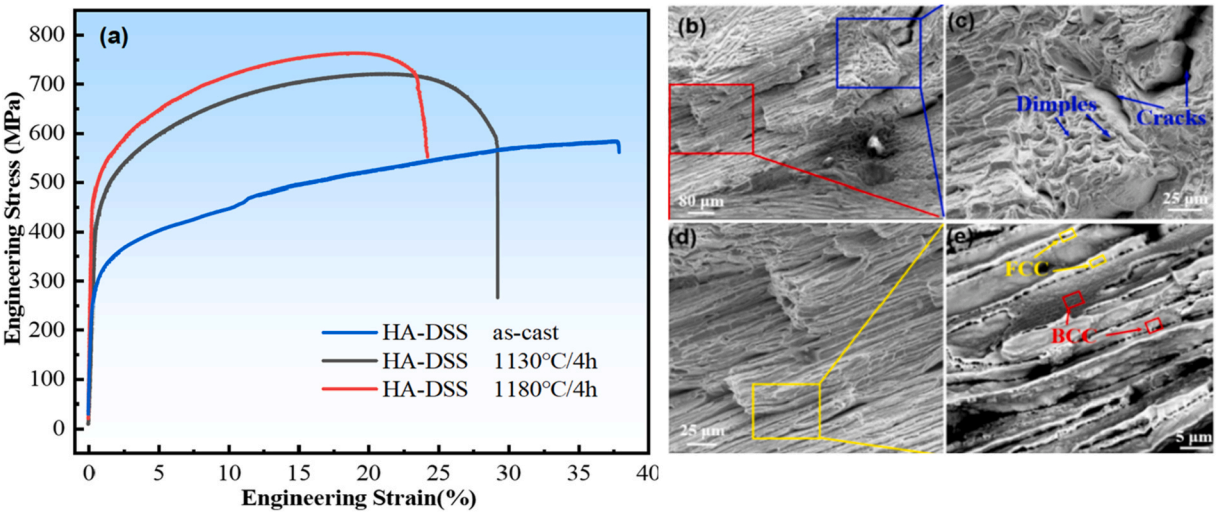

Fig. 5. (a)Engineering tensile stress-strain curves of the HA-DSS; (b-e) fractography of the HA-DSS after solution treatment at 1180 °C.

Table 2
Comparison of mechanical properties of reported DSS.

Steel grade	State	YS (MPa)	UTS (MPa)	TE (%)	Reference
2205-ASTM	hot rolled and annealed	450	655	25	[27]
2304-ASTM	hot rolled and annealed	400	600	25	[27]
00Cr22Ni6MnMoCu	solution treated	455	695	26.5	[28]
HA-DSS	solution treated	479	763	24	this work

accompanied by a decrease in ductility. This phenomenon can be attributed to the gradual phase transformation from the FCC phase to the BCC phase. For the sample that was solution treated at 1180 °C, the ultimate tensile strength reached 763 MPa with a total tensile elongation of 24%. Its fractography displayed in Fig. 5(b) reveals two distinct fracture features of the fibrous (shown in the red square) and dimple (shown in the blue square) zones [25]. In Fig. 5(c), several noticeable cracks surrounded by numerous dimples are evident, indicating the ductile fracture behavior which agrees with the material's good tensile elongation. Fig. 5(d) depicts a fibrous zone while the backscattered image in Fig. 5(e) reveals an alternating arrangement of dual phases. The hard BCC phase is less deformed while the soft FCC phase is stretched; the FCC phase then gradually becomes thinner and edges up, leaving the less deformed BCC phase at the bottom of the trench [26]. To better evaluate the mechanical performance of the HA-DSS alloy, Table 2 presents a comparison of the tensile properties of the present alloy with typical values of standard duplex stainless steels (e.g., 2205, 2304) based on ASTM specifications [27] and recent literature review [28]. It is worth noting that most reported values for conventional DSSs are based on hot-rolled and annealed conditions, as this is the typical

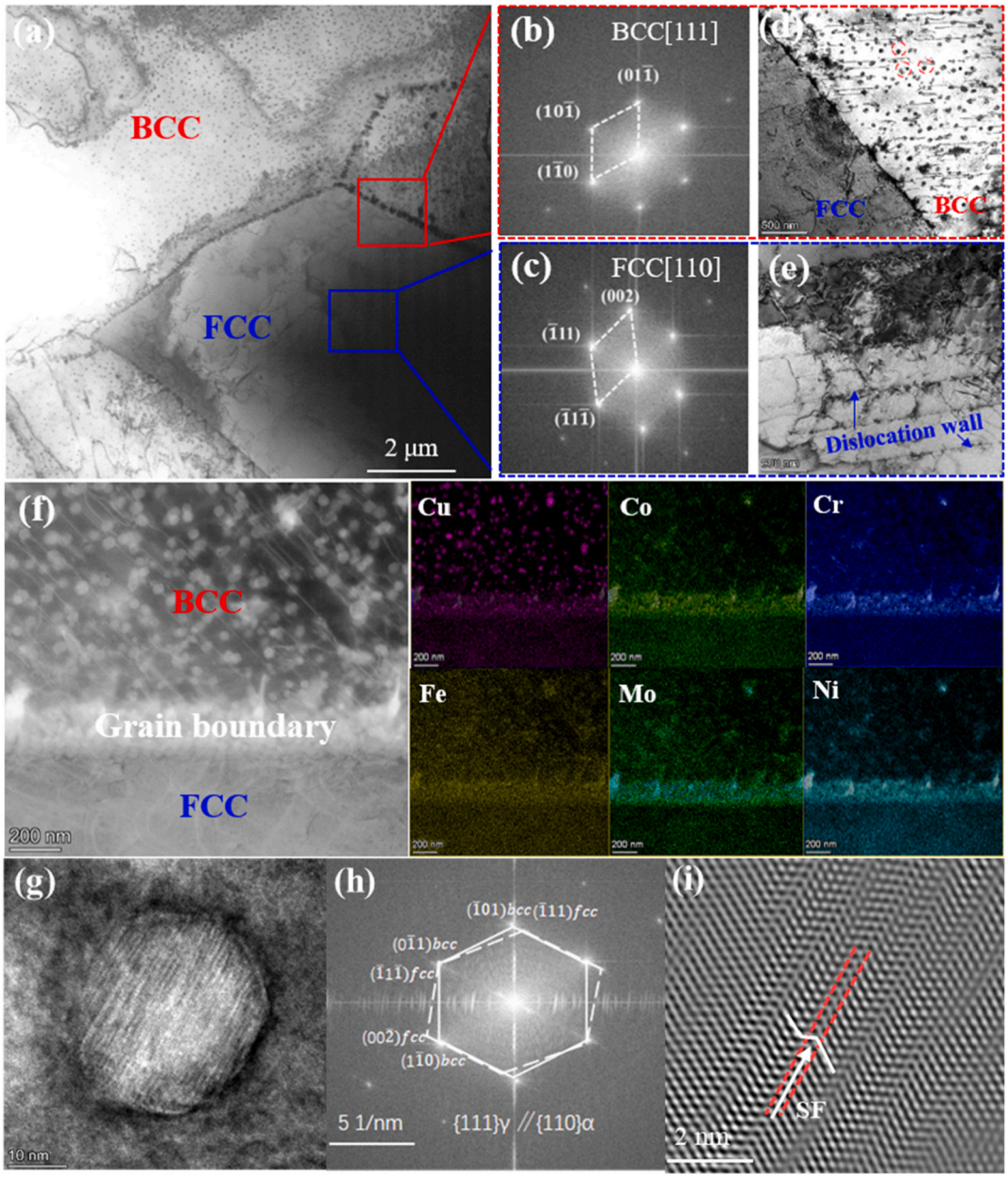

Fig. 6. TEM microstructure of the HA-DSS after solution treatment at 1180 °C: (a) an overall image; (b-c) SAED patterns of FCC and BCC phases; (d) nanoscale precipitates in the BCC phase near the FCC/BCC phase boundary; (e) dislocation walls within the FCC phase; (g-i) FTT and IFTT images of Cu-rich nanoscale precipitates.

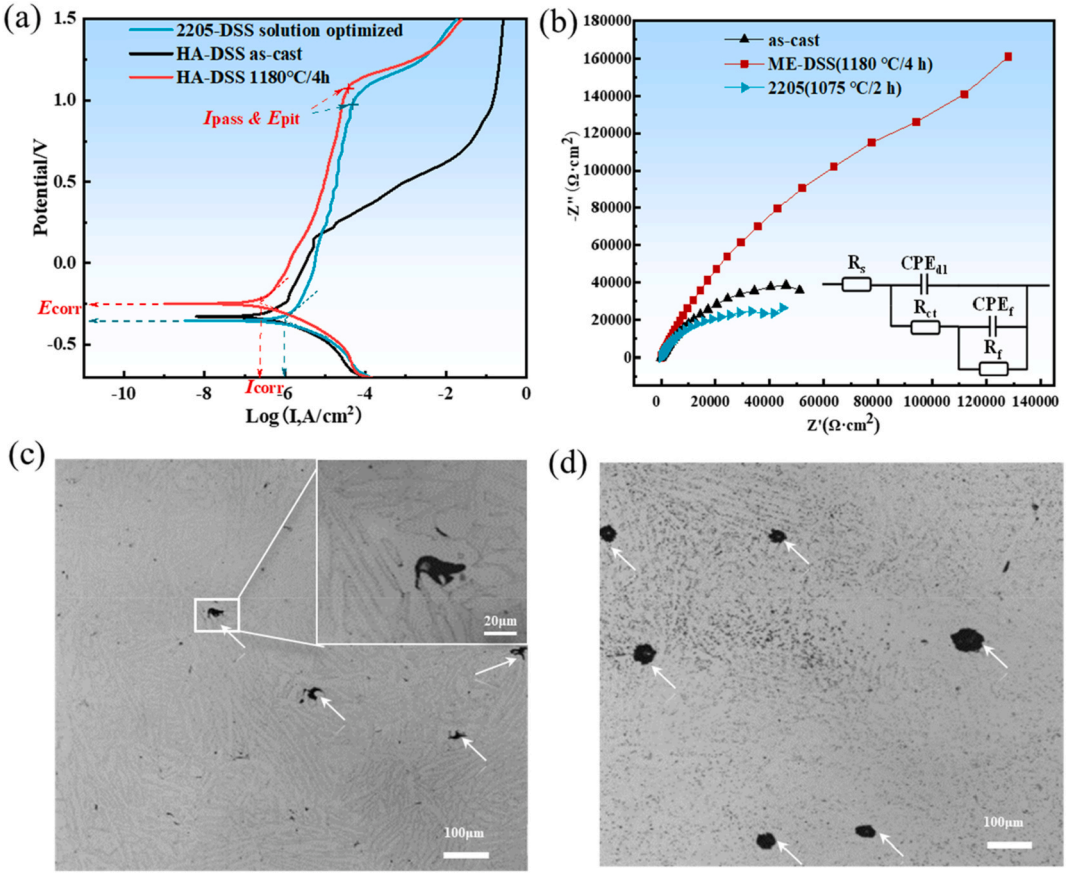

Fig. 7. (a) Polarization curves in 3.5 wt% NaCl solution; (b) Nyquist plots in 3.5 wt% NaCl solution with the fitted equivalent circuit shown in the inset; The morphology of corrosion pit in the solution treated (c) HA-DSS and (d) reference 2205-DSS.

processing route (solution treatment → rolling → annealing) [29–33]. By contrast, our HA-DSS samples are in the solution-treated state only yet already exhibiting mechanical properties comparable to those of industrially processed DSSs. This suggests that the HA-DSS alloy possesses huge potential in terms of mechanical properties, which may be further enhanced through optimized thermo-mechanical processing (e.g., cold/hot rolling and annealing), and warrants further investigations.

Fig. 6(a) provides the detailed TEM characterization of the sample after solution treatment at 1180 °C, revealing a uniform dispersion of numerous nano-precipitates in the BCC phase and dislocations within the FCC phase. The SAED patterns in Fig. 6(b–c) confirm the existence of both BCC and FCC phases. In Fig. 6(d), it is shown that the nano-precipitates are surrounded by dislocation lines in the BCC phase, particularly near the BCC/FCC phase interface. These dislocations can travel through the phase boundaries from the FCC phase into the BCC phase, where they are hindered by nanoscale precipitates. Fig. 6(e) presents parallelly aligned dislocation walls within the FCC phase, which are generally recognized for effectively inhibiting dislocation motion and improving the alloy strength [34].

The EDS mapping analysis in Fig. 6 (f) indicates that the nano-precipitates are enriched with Cu. The reason can be explained by the high positive mixing enthalpy between Fe and Cu. When a high content of Cu is dissolved in the high-temperature stable BCC phase, it tends to form a dense cluster of Cu atoms, which then precipitates as nanoscale phases during the subsequent cooling process. In Fig. 6(g), multiple stripes can be seen within the Cu-rich precipitates. Additionally, Fig. 6 (h–i) show the results of the Fast Fourier Transform (FFT) and inverse Fast Fourier Transform (IFFT) analyses of the precipitates. These results reveal two sets of diffraction spots with the FCC {111} planes being parallel to the BCC {110} planes, indicating a Kurdjumov-Sachs (KS) relationship; also, numerous stacking faults are formed in the nano-precipitates. Previous studies have highlighted that Cu-rich precipitates can enhance mechanical properties, improve corrosion resistance, reduce carbon content, and provide antibacterial properties in copper-containing steels [35–37]. Consequently, the strengthening mechanism of the HA-DSS can be attributed to the presence of multiple dislocations, and the existence of numerous Cu-rich nanoscale precipitates.

Table 3
Electrochemical parameters of HA-DSS and 2205-DSS polarization curves in 3.5 wt% NaCl solution and 10 wt% H_2SO_4.

Solution	Sample	E_{corr} (V vs. SCE)	i_{corr}(μA cm^{-2})	E_{pit} (V vs. SCE)	i_{corr}(μA cm^{-2})
3.5 wt% NaCl	As-cast	−0.329	0.399	0.144	5.01
	1180 °C	−0.250	0.299	1.09	41.789
	2205 (1075 °C)	−0.354	0.909	1.01	48.001
10 wt% H_2SO_4	As-cast	−0.264	40.504	0.902	204.17
	1180 °C	−0.230	15.33	0.907	77.62
	2205 (1075 °C)	−0.269	69.99	0.905	326.59

3.3. Corrosion resistance in NaCl and H_2SO_4 solutions

The polarization curves presented in Fig. 7(a) reveal that the as-cast HA-DSS exhibits relatively poor corrosion resistance and experiences rapid corrosion shortly after passivation in a 3.5% NaCl solution. In contrast, the passive region of both the solution-treated HA-DSS and the reference 2205-DSS is much wider, suggesting both materials

Table 4
Equivalent circuit fitting results of HA-DSS and 2205-DSS in 3.5 wt% NaCl solution.

Sample	R_S(Ω cm^2)	R_{ct}(Ω cm^2)	CPE_{dl}(Ω^{-1}cm^{-2}sn)	n_1	R_f (Ω cm^2)	CPE_f(Ω^{-1}cm^{-2}s^n)	n_2	C_f
As-cast	5.99	1.95×10^3	3.08×10^{-5}	0.91	1.16×10^5	5.99×10^{-5}	0.73	1.23×10^{-4}
1180 °C	6.34	1.81×10^4	2.89×10^{-5}	0.86	5.18×10^5	9.82×10^{-6}	0.66	2.27×10^{-5}
2205 (1075 °C)	5.41	4.11×10^3	6.10×10^{-5}	0.85	6.74×10^4	3.12×10^{-5}	0.67	4.50×10^{-5}

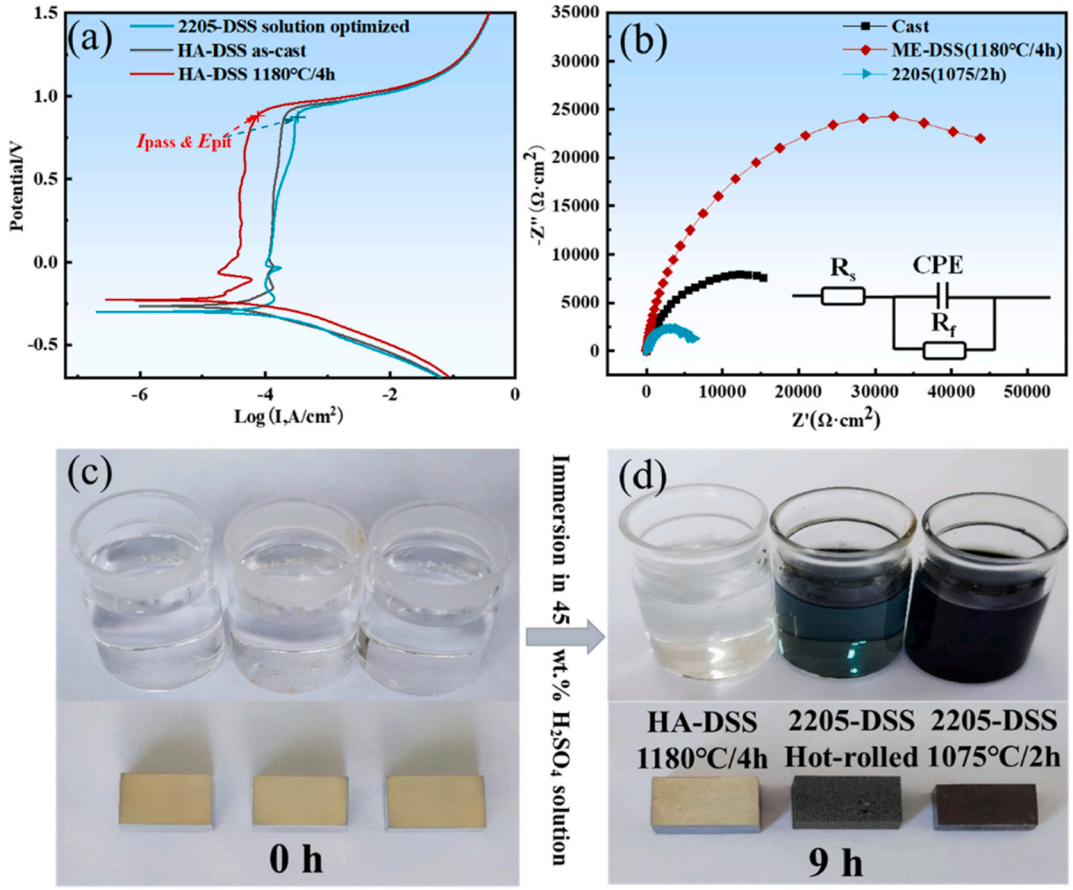

Fig. 8. (a) Polarization curves in a 10 wt% H_2SO_4 solution at 30 °C; (b) Nyquist plots with the fitted equivalent circuit shown in the inset; (c-d) Before and after immersion tests in a 45 wt% H_2SO_4 solution at 60 °C.

demonstrate improved corrosion resistance after solution treatment at the optimized temperature. The following values for the optimized solution-treated HA-DSS and 2205-DSS are compared, as shown in Table 3: corrosion potential (E_{corr}) is −0.250 V vs. −0.354 V, corrosion current density (I_{corr}) is 0.299 μA cm^{-2} vs. 0.909 μA cm^{-2}, passive current (I_{pass}) is 41.789 μA cm^{-2} vs 48.001 μA cm^{-2}, and critical pitting potential (E_{pit}) is 1.091 V vs.1.013 V. These results show that the HA-DSS has a less negative E_{corr}, a lower I_{corr} and I_{pass}, and a similar E_{pit}, demonstrating greater resistance to pitting corrosion than the reference 2205-DSS in the 3.5% NaCl solution. Fig. 7(b) shows the Nyquist plots, in which the solution-treated HA-DSS exhibits a larger capacitive-loop radius than the reference 2205-DSS. The equivalent circuit shown in the inset of Fig. 7(b) was used to fit the EIS results in the 3.5% NaCl solution, and the corresponding parameters are summarized in Table 4. In this model, R_s is the solution resistance, R_f and CPE_f correspond to the resistance and non-ideal capacitance of the passive film, respectively, while R_{ct} and CPE_{dl} represent the charge-transfer resistance and double-layer capacitance at the metal/film interface. Compared with the reference 2205-DSS, both R_f and R_{ct} increase markedly, with R_f approaching one order of magnitude and R_{ct} increasing by more than fourfold. This substantial enhancement indicates a much higher resistance to interfacial charge transfer, implying that the passive film formed on the solution-treated HA-DSS is denser and provides a stronger barrier effect against the penetration of aggressive Cl^- ions, thereby improving the resistance to chloride-induced pitting corrosion.

Fig. 7(c–d) compare the surface corrosion pits after the solution-treated samples were subject to potentiodynamic polarization at a kinetic potential of +1.6 V. The size and numbers of pits in the HA-DSS are much smaller and lower than those in the reference 2205-DSS, further confirming that the former has better pitting corrosion resistance. Additionally, the characteristics of the corrosion pits in the 2205-DSS are round, while those in the HA-DSS are irregular. The pitting in the HA-DSS occurs initially in the BCC phase and has an asymmetric shape which is constrained by the surrounding FCC phase. The preferential pitting in the BCC phase may be attributed to those Cu-rich nano-precipitates, leading to significant micro-galvanic corrosion within the BCC phase.

Fig. 8(a) displays the polarization curves for samples tested in a diluted 10 wt% H_2SO_4 solution at 30 °C. The key parameters derived from the polarization curves are presented in Table 3. The results indicate that the HA-DSS sample, after solution treatment at 1180 °C, exhibits greater corrosion resistance than the solution-treated reference 2205-DSS, with much lower I_{pass} and I_{corr} values. The latter only has similar E_{corr}, I_{corr}, and E_{pit} with the as-cast HA-DSS sample. Fig. 8(b)

Table 5
Equivalent circuit fitting results of HA-DSS and 2205-DSS in 10 wt% H_2SO_4.

Sample	R_S(Ω cm^2)	R_f(Ω cm^2)	*CPE* (Ω^{-1}cm^{-2}sn)	*n*	C_f
As-cast	0.87	1.93×10^4	1.61×10^{-4}	0.81	2.1×10^{-4}
1180 °C	0.93	5.84×10^4	9.88×10^{-5}	0.88	1.3×10^{-4}
2205 (1075 °C)	0.96	5.99×10^3	1.75×10^{-4}	0.84	1.8×10^{-4}

presents the Nyquist plots of the samples in 10 wt% H_2SO_4 solution. The Nyquist plot of the HA-DSS displays a significantly larger capacitive loop radius than that of the 2205-DSS, directly reflecting its superior passivation properties in the sulfuric acid environment. Unlike the pitting tendency observed in the 3.5 wt% NaCl solution, a single-time-constant equivalent circuit, shown in the inset of Fig. 8(b), was adopted to fit the EIS results. This suggests that the electrochemical response is dominated by a single interfacial process and is consistent with the presence of a relatively homogeneous passive film. As listed in Table 5, the passivation film resistance (R_f) of the HA-DSS after solution treatment reaches its maximum value of 5.84×10^4 Ω cm^2, which is nearly an order of magnitude higher than that of the 2205-DSS 5.99×10^3 Ω cm^2. In addition, the lower CPE/C_f values and slightly higher n value of the HA-DSS suggest a denser, smoother, and more stable passive film with fewer structural defects. This robust barrier strongly inhibits the acidic dissolution process. To further assess and compare the corrosion resistance of the solution-treated HA-DSS and 2205-DSS, the immersion result for them in a 45 wt% H_2SO_4 at 60 °C are presented in Fig. 8(c–d). The high concentration of sulfuric acid and elevated immersion

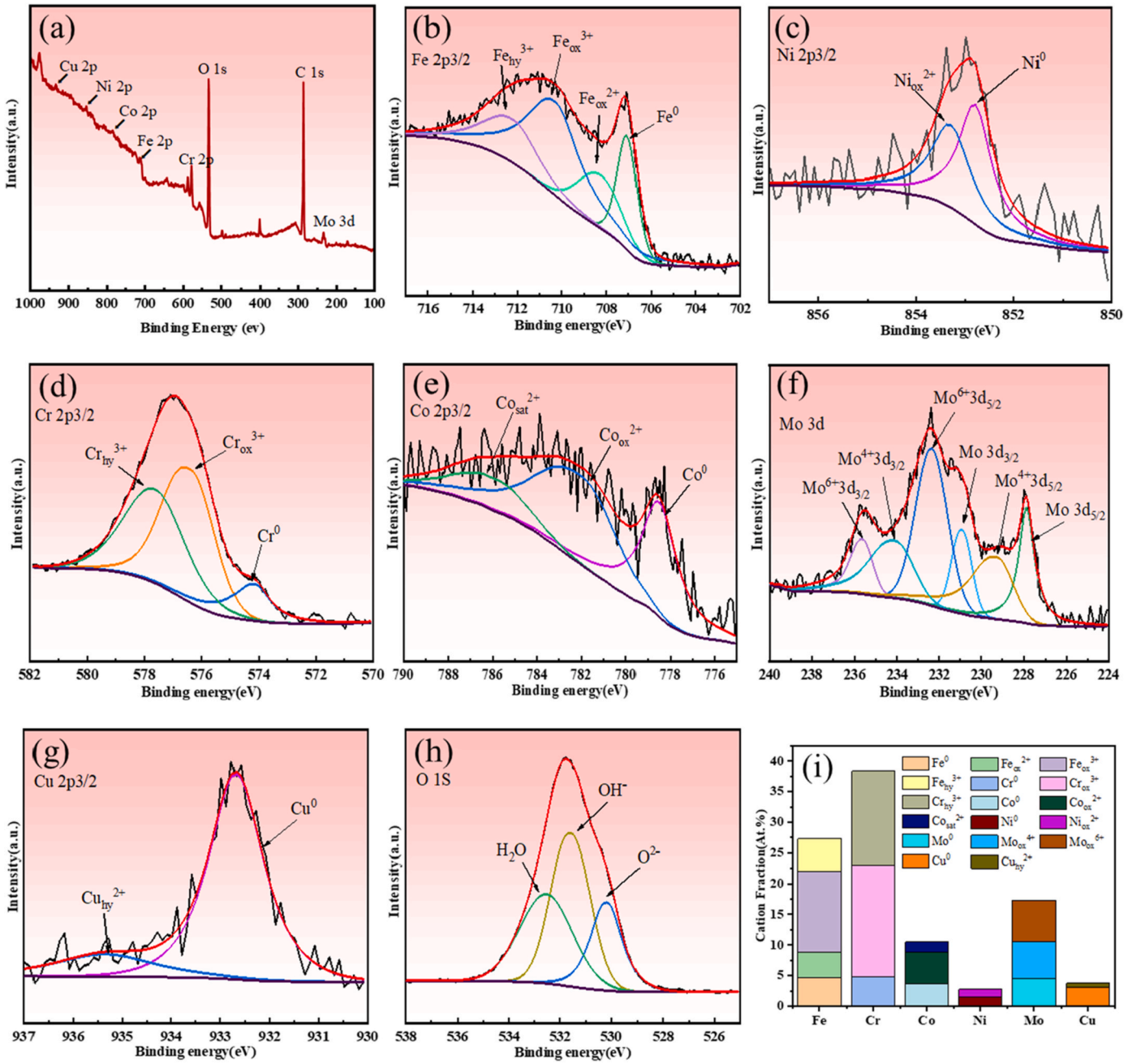

Fig. 9. XPS analysis of the passive film on the surface of the solution-treated (1180 °C/4h) HA-DSS after 10 days of immersion in a 10 wt% H_2SO_4 solution at ambient temperature.

temperature were intentionally employed to accelerate the corrosion process, and a commercially purchased hot-rolled 2205-DSS sample was also included in the comparison. Obviously, after 9 h of immersion, only slight surface changes were observed for the solution-treated HA-DSS after immersion, and the sample surface remained relatively bright. In comparison, after the same immersion time, the color of the sulfuric acid solution containing the hot-rolled 2205-DSS darkened, and the size of the solution-treated 2205-DSS sample greatly decreased due to corrosion. Before immersion, the compared samples had similar dimensions, whereas after immersion the solution-treated 2205-DSS showed a pronounced reduction in size. Based on the measured post-corrosion dimensions, the apparent volume reduction was estimated to be about 40%. The hot-rolled 2205-DSS demonstrated only slightly better corrosion resistance compared to the laboratory prepared solution-treated 2205-DSS, indicating that the newly developed HA-DSS in this work has potential for further improvement of its overall performance after subsequent processing like hot-rolling.

To clarify the mechanism for the high corrosion resistance of the solution-treated HA-DSS in the H_2SO_4 solution, Fig. 9 presents the XPS analysis of the passive film on the HA-DSS after solution treatment at 1180 °C for 4h, which retains a metallic luster without visible corrosion products after immersion in a 10% H_2SO_4 at ambient temperature for 10 days. Fig. 9(a) presents the XPS survey spectrum, which confirms that all major alloying elements are involved in the formation of the passive film. The spectra for Fe 2p3/2, Ni 2p3/2, Cr 2p3/2, Co 2p3/2, Mo 3d, Cu 2p3/2, and O 1s were fitted as shown in Fig. 9(b–h), based on the peak parameters presented in previous literatures [38]. The spectrum of O consists of three peaks: H_2O, OH^-, and O^{2-}. O^{2-} corresponds to the formation of metal oxides, while OH^- exists in the form of hydroxides. These findings demonstrate that metallic hydroxides and oxides are the primary constituents of the passive film. The presence of H_2O can capture metal ions in the solution [39], forming a new film on the surface of the passive film and improving the corrosion resistance of the alloy [40]. Fig. 9(h) presents the quantitative atomic ratio (C_x) of each element in the passivation film calculated using the following equation [41]: $C_x = (I_x/S_x)/(\sum I_x/S_x)$,where I_x denotes the peak area of each element and S_x refers to the sensitivity factor derived from the XPS instrument. It is seen that Cr and Fe are the most predominant elements in the passive film of the solution-treated HA-DSS, which also indicates that the phase structure of this passive film is similar to that of conventional stainless steels. As a result, their E_{pass} values are nearly identical to those of the reference 2205-DSS both in NaCl and H_2SO_4 solutions, as shown in Figs. 7(a) and 8(a). The main difference firstly lies in the Cr/Fe ratio. In previous literatures [42,43], the Cr/Fe ratio typically ranges from 0.5 to 1.5, and it is believed that a high ratio improves the corrosion potential and reduces the corrosion rate. The passive film of the solution-treated HA-DSS contains 38.35% Cr ions and 27.31% Fe ions (Cr/Fe ration about 1.4), with Cr_{hy}^{3+} accounting for 15.25%. The presence of a significant amount of Cr_{hy}^{3+} also helps inhibit Cl^- penetration and reduces the rate of anodic dissolution. Secondly, the passive film has a relatively high Mo content, with Mo_{ox}^{6+} and Mo_{ox}^{4+} both exceeding 6%. It is well known that Mo is the critical element for improving the corrosion resistance in traditional stainless steel. Previous studies suggested that Mo_{ox}^{6+} accumulates on the surface of the passive film, while Mo_{ox}^{4+} is present internally, effectively preventing ion erosion [44]. Additionally, the presence of Co and Cu in the solution-treated HA-DSS also enhances the passive film. Co primarily exists as Co_{ox}^{2+}, while Cu remains in its metallic state. CoO and Cr_2O_3 can further form the spinel oxide $CoCr_2O_4$ [45], and Cu tends to reduce the iron oxide content while increasing the chromium oxide content in the passive film [38]. The formation of Cr_2O_3 and $CoCr_2O_4$ contributes to creating a denser passive film, thereby enhancing its stability and hence the corrosion resistance. The relative fractions of the fitted chemical states for each alloying element are summarized in Fig. 9(i).

4. Conclusion

(1) The newly designed $Fe_{60}Cr_{18}Co_6Ni_6Mo_6Cu_4$ HA-DSS follows a solidification path similar to that of conventional duplex stainless steels: L → L + BCC → BCC → BCC + FCC. With increasing solution-treatment temperature, the phase balance evolved progressively, and at 1180 °C the alloy reached an approximately balanced duplex microstructure with BCC and FCC phase fractions of about 54% and 46%, respectively.

(2) The optimized HA-DSS after solution treatment at 1180 °C exhibited a tensile strength of 763 MPa and an elongation of 24%. Its strengthening behavior is associated with the coexistence of high-density dislocations in the FCC phase and nanoscale Cu-rich precipitates in the BCC phase.

(3) The optimized HA-DSS showed superior corrosion resistance to commercial 2205-DSS in both chloride- and acid-containing environments. In 3.5 wt% NaCl solution, the HA-DSS exhibited $E_{corr} = -0.250$ V, $I_{corr} = 0.299$ μA cm^{-2}, and $E_{pit} = 1.09$ V, compared with −0.354 V, 0.909 μA cm^{-2}, and 1.01 V for 2205-DSS. In 10 wt % H_2SO_4 solution, the HA-DSS showed $E_{corr} = -0.230$ V and $I_{corr} = 15.33$ μA cm^{-2}, whereas 2205-DSS showed −0.269 V and 69.99 μA cm^{-2}.

(4) XPS analysis revealed that the passive film formed on HA-DSS contains a complex mixture of Fe-, Cr-, Co-, Mo-, and Cu-containing oxides/hydroxides, indicating that the additional alloying elements contribute synergistically to passive-film stability and corrosion resistance.

Declaration of competing interest

The authors declare that they have no known competing financial interests or personal relationships that could have appeared to influence the work reported in this paper.

Acknowledgement

This work was financially supported by the National Natural Science Foundation of China (Grant No.51971001), and Key Research and Development Project of Anhui Province (Grant No.2022a05020017).

References

[1] Zhao S, Wang L. Formation and properties of nitrided layer on 2205 duplex stainless steel by anodic plasma-nitriding assisted with hollow cathode discharge. J Mater Res Technol 2024;31:3652–60.
[2] Xie XF, Jiang W, Liu R, Wan Y, Zhang Q, Wang L, Du Y. Evolution of phase ratio and its effect on residual stress for 2205 duplex stainless steel multipass welded joints by thermo-metallurgical-mechanical model. Int J Pres Ves Pip 2024;211:105283.
[3] Jinlong L, Tongxiang L, Chen W, Limin D. Effect of ultrafine grain on tensile behaviour and corrosion resistance of the duplex stainless steel. Mater Sci Eng, C 2016;62:558–63.
[4] Zhang Y, Wang C, Reddy KM, Li W, Wang X. Study on the deformation mechanism of a high-nitrogen duplex stainless steel with excellent mechanical properties originated from bimodal grain design. Acta Mater 2022;226:117670.
[5] Pan M, Zhang J, Zhang X. Effect of Cu addition on phase fraction, mechanical properties and corrosion properties of Fe–Cr–Mn–Al duplex stainless steel. Mater Sci Eng 2022;857:144095.
[6] Yoon BJ, Ahn YS. Effect of Mo addition on aging behavior of TRIP-aided duplex stainless steel. Mater Charact 2021;173:110946.
[7] Chen G, Xu G, Biermann H, Mola J. Microstructure and mechanical properties of Co-added and Al-added austenitic stainless steels. Mater Sci Eng A 2022;854:143832.
[8] Nilsson JO. Super duplex stainless steels. Mater Sci Technol 1992;8(8):685–700.
[9] Chail G, Kangas P. Super and hyper duplex stainless steels: structures, properties and applications. Procedia Struct Integr 2016;2:1755–62.
[10] Wang W, Mu W, Wei D, Wu H, Yu L, Jonsson T, Larsson H, Mao H. High corrosion resistance duplex fcc + hcp cobalt based entropic alloys: an experimental and theoretical investigation. Mater Des 2022;223:111166.
[11] Lim KR, Kwon HJ, Kang JH, Won JW, Na YS. A novel ultra-high-strength duplex Al–Co–Cr–Fe–Ni high-entropy alloy reinforced with body-centered-cubic ordered-phase particles 2020;771:138638.

[12] Luo L, Liu SJ, Shi W, Fu H, Liu F, Xiang S. The formation mechanism of the nano-equiaxed (α+β) duplex phases structure during aging process after high pressure torsion deformation. Mater Today Commun 2024;40:109788.
[13] Xu S, Han Y, Sun J, Zu G, Jiang M, Zhu W, Ran X. Designing gradient nanograined dual-phase structure in duplex stainless steel for superior strength-ductility synergy. J Mater Sci Technol 2024;170:122–8.
[14] Tian J, Chen B, Wu Y, Pang J, Cao T, Jiang F. Microstructural evolution and duplex structure-enhanced high-temperature mechanical properties of Al-doped VCoNi medium entropy alloy. J Alloys Compd 2023;965:171322.
[15] Zhang H, Tang H, Li WH, Wu JL, Zhong XC, Chen G, Guo S. Novel high-entropy and medium-entropy stainless steels with enhanced mechanical and anti-corrosion properties. Mater Sci Technol 2018;34(5):572–9.
[16] Dou B, Zhang H, Tao Y, Ma QS, Guo S. Effect of Fe content on type and distribution of carbides in medium-entropy high-speed steels. Tungsten 2023;5(1):189–97.
[17] Xu BQ, Zhang H, Ma D, Ma QS, Pei LZ. Ageing hardening mechanism and corrosion resistance in the $Fe_{65}Cr_{13}Cu_3(CoMnMoNiAlTi)_{19}$ medium-entropy stainless alloy. Acta Metall Sin-engl 2021;34(11):1601–8.
[18] Guo S, Ng C, Lu J, Liu CT. Effect of valence electron concentration on stability of fcc or bcc phase in high entropy alloys. J Appl Phys 2011;109(10):103505.
[19] Garfinkel DA, Poplawsky JD, Guo W, Young GA, Tucker JD. Phase separation in lean-grade duplex stainless steel 2101. JOM 2015;67(10):2216–22.
[20] Zhang J, Hu X, Lin P, et al. Effect of solution annealing on the microstructure evolution and corrosion behavior of 2205 duplex stainless steel. Mater Corros 2019;70(4):676–87.
[21] Tütük İ, Ural MM, Özer G, et al. Influence of solution treatment process on the properties of duplex stainless steels: a comparative study on microstructure and corrosion properties of UNS S32205 and UNS S32760. Metall Mater Trans B 2024;55:2916–21.
[22] Sung CW, Shin BH, et al. Effect of solution annealing on austenite morphology and pitting corrosion of super duplex stainless steel UNS S32750. Int J Electrochem Sci 2021;16(8):210813.
[23] Hsieh CC, Wu W. Overview of intermetallic sigma (σ) phase precipitation in stainless steels. Int Sch Res Not 2012;2012:1–16.
[24] Sieurin H, Sandström R. Sigma phase precipitation in duplex stainless steel 2205. Mater Sci Eng 2007;444(1):271–6.
[25] Jarrahi M, Blöcher G, Kluge C, Holländer HM. Elastic-plastic fracture propagation modeling in rock fracturing via punch through shear test. Rock Mech Rock Eng 2021;54(6):3135–47.
[26] Lu YP, Gao XZ, Jiang L, Chen ZN, Wang TM, Jie JC, Kang HJ, Zhang YB, Guo S, Ruan HH, Zhao YH, Cao ZQ, Li TJ. Directly cast bulk eutectic and near-eutectic high entropy alloys with balanced strength and ductility in a wide temperature range. Acta Mater 2017;124(2):143–50.
[27] Kahar S. Duplex stainless steels-an overview 2017;7:27–36.
[28] Bao R, Rodrigues EB, Guo C, Xu Z. Preparation and erosion resistance properties of 00Cr22Ni6MnMoCu duplex stainless steel. Results Eng 2025;26:105004.
[29] Liu ZH, Han Y, Wu ZG, Sun JP, Zu GQ, Zhu WW, Ran X. Microstructures and mechanical properties of cold-rolled 21Cr lean duplex stainless steel with medium to high cold rolling reductions. Mater Today Commun 2022;33:104860.
[30] Moallemi M, Hanzaki AZ, Kim SJ, Hong C, Nezhadfar PD. Deformation behavior of a high-plasticity nano/ultrafine-grained N-bearing duplex stainless steel: twin/twin-like induced plasticity effect. Mater Sci Eng 2017;700:637–40.
[31] Chen M, Li J, Liu H, Wang M, Xing S, Zhao Y. Achievement of high strength-ductility combination in austenitic and ferritic duplex stainless steel by heterogeneous deformation. J Mater Res Technol 2022;21:943–50.
[32] Li W, Li J, Gong Q, Guo H, Cao Z, Mu W. Annealing parameters effect on microstructure evolution, tensile properties and deformation behaviors of direct-cold-rolled UNS S32101 duplex stainless steel with heterogeneous layered structure. Mater Sci Eng 2023;883:145439.
[33] Ghosh SK, Mahata D, Roychaudhuri R, Mondal R. Effect of rolling deformation and solution treatment on microstructure and mechanical properties of a cast duplex stainless steel. Bull Mater Sci 2012;35(5):839–46.
[34] Liu XX, Ma SG, Song WD, Zhao D, Wang ZH. Microstructure evolution and mechanical response of Co-free $Ni_2CrFeAl_{0.3}Ti_x$ high-entropy alloys. J Alloys Compd 2023;931:167523.
[35] Wang J, Jiang H, Chang X, Zhang L, Wang H, Zhu L, Qin S. Effect of Cu content on the microstructure and corrosion resistance of $AlCrFeNi_3Cu_x$ high entropy alloys. Corros Sci 2023;221:111313.
[36] Hättestrand M, Nilsson JO, Stiller K, Liu P, Andersson M. Precipitation hardening in a 12%Cr-9%Ni-4%Mo-2%Cu stainless steel. Acta Mater 2004;52(4):1023–37.
[37] Han G, Shang CJ, Misra RDK, Xie ZJ. Solid phase transition of Cu precipitates in a low carbon TRIP assisted steel. Phys Rev B Condens 2019;569:68–79.
[38] Gao X, Wang H, Ma C, Lv M, Sha G, Li Y, Ren H. Micromechanism involved in ultrafine grained ferrite/martensite dual phase steels strengthened by nanoscale Cu-rich precipitates. Mater Sci Eng 2021;819:141522.
[39] Asami K, Hashimoto K, Shimodaira S. XPS determination of compositions of alloy surfaces and surface oxides on mechanically polished iron-chromium alloys. Corros Sci 1977;17(9):713–23.
[40] Okamoto GO, Shibata T. Desorption of tritiated bound-water from the passive film formed on stainless steels. Nature 1965;206(4991):1350. 1350.
[41] Xu ZL, Zhang H, Du XJ, He YZ, Luo H, Song GS, Mao L, Zhou TW, Wang LL. Corrosion resistance enhancement of CoCrFeMnNi high-entropy alloy fabricated by additive manufacturing. Corros Sci 2020;177:108954.
[42] Yue Y, Liu C, Shi P, Jiang M. Passivity of stainless steel in sulphuric acid under chemical oxidation. Corrosion Eng Sci Technol 2018;53(3):173–82.
[43] Zhao K, Li XQ, Wang LW, Yang QR, Cheng LJ, Cui ZY. Passivation behavior of 2507 super duplex stainless steel in hot concentrated seawater: influence of temperature and seawater concentration. Acta Metall Sin-engl 2021;35(2):326–40.
[44] Olsson COA, Landolt D. Passive films on stainless steels-chemistry, structure and growth. Electrochim Acta 2003;48(9):1093–104.
[45] Liu F, Song Q, Chen R, Wang C, Sun J. Effect of Co, Ni, Cu content on phase composition, microstructure and corrosion resistance of $Co_{1-x}CrFeNi_{1+x}Cu_y$ series high-entropy alloys. Vacuum 2023;210:111830.